Research Square

Preprints are preliminary reports that have not undergone peer review.
They should not be considered conclusive, used to inform clinical practice,
or referenced by the media as validated information.

Single-Scan Three-Dimensional Atomic Imaging via Electron Ptychographic Interferometry

Wu Zhou

wuzhou@ucas.ac.cn

University of Chinese Academy of Sciences https://orcid.org/0000-0002-6803-1095

Ang Li

University of Chinese Academy of Sciences https://orcid.org/0009-0002-5967-0626

Shuoyuan Huang

University of Chinese Academy of Sciences

Yinhang Ma

University of Chinese Academy of Sciences

Tong Liu

University of Chinese Academy of Sciences

Zhaoqing Wang

University of Chinese Academy of Sciences https://orcid.org/0009-0005-9043-894X

Jingbo Pang

University of Chinese Academy of Sciences

Stephen Pennycook

School of Physical Sciences, University of Chinese Academy of Sciences

Hong-Jun Gao

Institute of Physics, Chinese Academy of Sciences https://orcid.org/0000-0001-9323-1307

Article

Keywords:

Posted Date: April 14th, 2026

DOI: https://doi.org/10.21203/rs.3.rs-9384287/v1

License: This work is licensed under a Creative Commons Attribution 4.0 International License.
Read Full License

Additional Declarations: There is **NO** Competing Interest.

Single-Scan Three-Dimensional Atomic Imaging via Electron Ptychographic Interferometry

Ang Li[1#], Shuoyuan Huang[1#], Yinhang Ma[1#,†], Tong Liu[1], Zhaoqing Wang[1], Jingbo Pang[1], Stephen J. Pennycook[1], Hong-Jun Gao[1,2], Wu Zhou[1*]

[1]School of Physical Sciences, University of Chinese Academy of Sciences, Beijing, China

[2]Institute of Physics, Chinese Academy of Sciences, Beijing, China

[†]Present address: School of Materials and Energy, University of Electronic Science and Technology of China, 611731, Chengdu, China

[#] These authors contributed equally: Ang Li, Shuoyuan Huang, Yinhang Ma.

[*] Corresponding author: wuzhou@ucas.ac.cn

Abstract:

Resolving atomic positions in all three dimensions with high precision is central to understanding many emergent properties of quantum materials, but has remained fundamentally challenging. Existing three-dimensional (3D) imaging methods in electron microscopy are largely tomography-based, relying on geometrical parallax from tilt-series projections and high electron doses, which makes them unfriendly for beam-sensitive and structurally flexible systems such as 2D materials. Here, we introduce electron ptychographic interferometry (EPI), a single-scan 3D atomic imaging method that exploits intrinsic wave interference induced by individual atoms during electron scattering. By decoding this atom-induced interference in the amplitude of the electron exit wave into a quantitative depth-sensitive contrast, EPI retrieves full 3D atomic coordinates with picometer axial precision and deep sub-angstrom lateral resolution, without specimen tilting or model assumptions. We validate the picometer accuracy of EPI by quantifying the 2.98 Å S-S interlayer distance in monolayer MoS_2, and apply it to experimentally resolve, for the first time, a ~5 pm out-of-plane structural

reconstruction in AA-stacked regions of magic-angle twisted bilayer graphene. EPI thus establishes a physically distinct and experimentally accessible route to single-scan 3D atomic imaging, opening new opportunities to uncover atomic-scale origins of quantum phenomena.

Determining the three-dimensional (3D) atomic structure is essential for understanding the functionality of quantum materials[1-3]. Even in two-dimensional (2D) materials and their heterostructures[4-8], where atoms are confined to quasi-2D planes, picometer-scale out-of-plane atomic displacements can profoundly modulate interlayer coupling, thereby reshaping strain distributions and electronic correlations[1,2,9]. Twisted bilayer graphene (tBLG) provides a prominent example, in which theoretical studies predict that subtle in-plane and out-of-plane structural reconstructions at the picometer scale play a decisive role in its emergent superconductivity and corelated insulating states[10-14]. Although recent advances in electron microscopy and Bragg interferometry have enabled high precision mapping of in-plane lattice distortions[14-17], direct and quantitative experimental measurements of these critical out-of-plane atomic displacements remain elusive, leaving a fundamental gap between theoretical prediction and experimentally resolved atomic structures[10-13].

The challenge of retrieving high-precision out-of-plane atomic information originates from the projection approximation inherent to conventional atomic-resolution electron microscopy[18,19]. Under this long-standing assumption, the electron exit wave is considered to encode structural information solely through the projected electrostatic potential of the specimen[20,21], thereby effectively eliminating sensitivity to atomic depth. Consequently, despite aberration-corrected scanning transmission electron microscopy (STEM) [21-23] and electron ptychography[24-28] can now readily achieve deep sub-angstrom lateral resolution, their axial sensitivity remains limited to several nanometers[25,29-32], orders of magnitude poorer than required to resolve picometer scale out-of-plane atomic displacements. Methods such as atomic electron tomography (AET)

[33-36] and ptychographic atomic electron tomography(pAET) [37-39] can, in principle, access the third dimension[40], but require extensive tilt-series acquisition, high electron doses and computationally intensive reconstructions. These requirements render them unsuitable for beam-sensitive and structurally flexible 2D materials, in which irradiation damage and dynamic structural relaxation during multi-tilt acquisition can obscure the intrinsic atomic configuration. A method capable of retrieving full 3D atomic coordinates from a single image acquisition, without imposing geometric constraints or prior structural models, is therefore critically needed.

In this work, we introduce **electron ptychographic interferometry (EPI)**, a single-scan coherent imaging method that converts atom-induced interference effects into a high-precision, depth-sensitive imaging contrast. We show that the electron exit wave in coherent imaging encodes not only the projected electrostatic potential in its phase, but also quantitative depth information contained in previously overlooked amplitude variations. By quantitatively analyzing the amplitude-phase coupling in ptychographic reconstructions, EPI extracts a new contrast that uniquely determines axial atomic positions with picometer precision. We first demonstrate this capability by resolving the 3D atomic structure of monolayer MoS_2, accurately retrieving the 2.98 Å S-S interlayer distance. Crucially, EPI directly addresses the long-standing out-of-plane structural reconstruction problem in magic-angle tBLG, revealing previously unobserved ~5 pm out-of-plane structural relaxations in the AA-stacked regions with a precision better than 3 pm. Furthermore, we demonstrate the generality of EPI in a wider range of material problems by resolving the 3D bonding configuration of individual dopant atoms and visualizing surface atomic layers. Together, these results establish EPI as a physically distinct, experimentally accessible and broadly applicable approach for single-scan 3D atomic imaging, providing a new pathway for uncovering the atomic-scale origins of emergent quantum phenomena.

Physical principle of electron ptychographic interferometry

Electron ptychography reconstructs the complex exit wave of an electron beam scattered by a specimen, which is typically interpreted as a projected phase image under the projection and phase-object approximations[18,19]. These assumptions hold when all atoms are confined to a single plane, such that amplitude variations in the exit wave are negligible. However, with the extreme coherence of modern electron sources, atomic scattering introduces local curvature to the electron wavefront, giving rise to pronounced interference between the incident and scattered wave components that is intrinsically sensitive to picometer-scale axial atomic displacements. This interference produces a coupled modulation of both the amplitude and phase of the reconstructed exit wave—an effect that encodes quantitative depth information but has long been overlooked and commonly dismissed as experimental noise.

To illustrate this phenomenon, we simulated the propagation of a 60 kV electron probe near its focal plane (see **Supplementary Note 1**). In vacuum, the amplitude of the probe wavefunction on the optical axis decays only slightly, by ~10% over an axial propagation distance of 2.4 nm **(Supplementary Fig. 1**), reflecting the near-planarity of the wavefront and defining the nanoscale depth-of-field that fundamentally limits the depth resolution in conventional STEM. In contrast, when the electron beam interacts with an atom, the phase delay induced by the atomic potential acts as a weak convex lens, locally curving the wavefront and inducing strong self-interference (**Fig. 1a**). This interference redistributes the wave intensity, producing an on-axis amplitude enhancement over 20% within 0.2 nm of propagation from the atom (**Fig. 1b**), in stark contrast to vacuum propagation. When the exit wave is instead evaluated at a plane located upstream of the atom, the principle of reversibility dictates that the amplitude change relative to the atom plane reverses sign. In this scenario, the interaction can be interpreted as the atom effectively introducing a divergent wavefront curvature in the backward direction, resulting in rapid amplitude attenuation (blue dashed lines in **Fig. 1b**). Importantly, these pronounced on-axis amplitude variations arise from interference-induced intensity redistribution, and their strong dependence on axial

position provides a unique interferometric fingerprint of atomic depth that cannot be captured by conventional phase-object or projection approximations.

Further simulations show that the amplitude redistribution can directly quantify the depth information after decoupling the phase contribution. The magnitude of the amplitude modulation increases near-monotonically with propagation distance, whereas the corresponding phase shift gradually decreases along the optical axis (**Supplementary Fig. 2, Supplementary Figs. 3a, b**). Normalizing the amplitude change by the corresponding phase shift removes variations arising from differences in atomic potential strengths and propagation-induced phase modulation. The resulting normalized amplitude change exhibits a near-proportional dependence on propagation distance (**Supplementary Figs. 3c**) across a wide range of atomic potentials and experimental parameters (**Supplementary Figs. 4**). By reciprocity, this propagation-distance-dependent amplitude response can be equivalently observed by varying the axial position of an atom while detecting the exit wave at a fixed reference plane (**Supplementary Note 1**). In this configuration, the normalized amplitude change scales directly with the atom's z coordinate, establishing a quantitative and monotonic relationship between amplitude modulation and atomic axial position (**Fig. 1c)**.

This mechanistic insight motivates our proposal of EPI. In conventional electron ptychography, the object transmission function $O(r)$ is reconstructed from the recovered exit wavefunction $\psi_{exit}(r, R_j)$ at each probe position R_j (**Fig. 1d)**. As discussed above, the amplitude of $O(r)$ inherently contains information about the atomic axial positions with picometer-level sensitivity, but this information has so far been largely overlooked. EPI explicitly extracts this atomic z-coordinate information by defining an EPI contrast, $EPI\ (r) = [A(r) - 1] \times \phi(r)$, where $A(r)$ and $\phi(r)$ denote the amplitude and phase of the reconstructed object function, respectively. This formulation preserves the depth sensitivity carried by the amplitude component while suppressing background noise in regions between atoms. In addition, the multiplication

operation sharpens atomic peaks, resulting in enhanced lateral spatial resolution compared to conventional ptychographic phase imaging (**Supplementary Fig. 5**). At individual atomic positions, the EPI signal scales as $EPI \propto z \times \phi^2$, enabling direct z-coordinate retrieval from a single ptychography reconstruction.

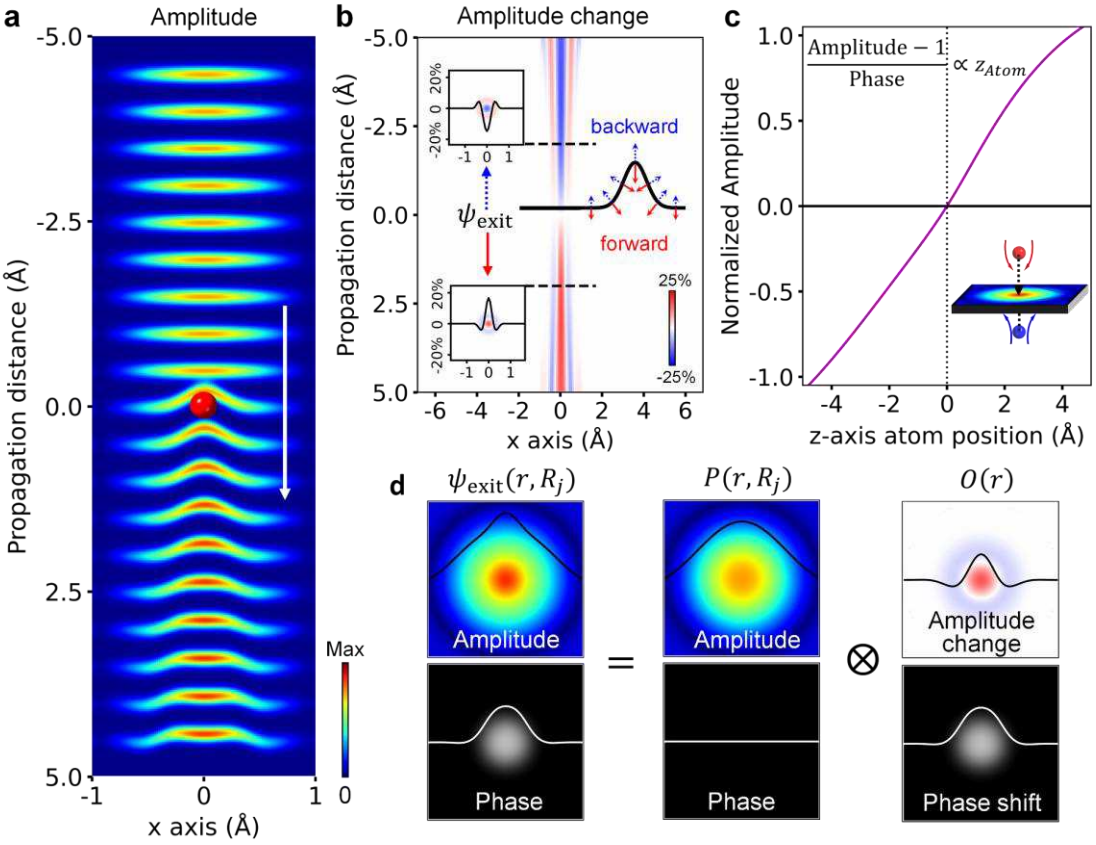


Figure 1. Physical principle of electron ptychographic interferometry (EPI). **a**, Simulation of an electron wavefront propagating in the vicinity of an atom (red sphere). The atomic potential induces a local phase delay that curves the wavefront, analogous to the action of a weak convex lens. **b**, Atom-induced amplitude modulation of the exit wave on the optical axis compared with vacuum propagation. Left insets show cross-sections of the wave amplitude for backward (upper) and forward (lower) propagation by 2 Å from the atomic plane. Right inset schematically illustrates the convergence and divergence of the curved wavefront during the forward (red arrows) and backward (blue arrows) propagations. **c**, Near-linear dependence of the normalized amplitude change (amplitude change divided by the corresponding phase shift) on the atomic position

along the z-axis. Inset illustrates the opposite interference behavior for atoms located above and below the reference plane. **d**, Conceptual schematic of EPI. When atoms are axially displaced from the reference plane, the amplitude of the ptychographically reconstructed object function, $O(r)$, encodes depth information. EPI extracts this information to retrieve full 3D atomic coordinates from a single image scan.

EPI contrast and implementation

We first demonstrate the EPI method on a twisted bilayer graphene (tBLG) sample with a controlled twist angle of $\sim 1°$. **Figures 2a-b** compare a conventional ptychographic phase image with the corresponding EPI image reconstructed from the same 4D-STEM dataset. The phase image achieves deep-sub-angstrom lateral resolution with individual atomic columns clearly resolved, but contains no depth information. In contrast, the EPI image exhibits both enhanced lateral resolution and opposite contrast signs for carbon atoms located above and below a reference plane defined by the reconstruction, providing a direct visualization of their relative axial (z) positions.

Quantitively, the lateral resolution improves from 0.46 Å in the phase image to 0.31 Å in the EPI image. Notably, this 0.31 Å resolution surpasses the reported resolution record for electron ptychography when the electron wavelength is taken into account (**Supplementary Table 1**). In the saddle-point (SP) stacked regions, where carbon atoms from the two graphene layers are laterally displaced in projection, the conventional phase image resolves individual atoms but cannot distinguish which graphene layer each carbon atom belongs to (**Fig. 2c**). The EPI image, however, displays opposite contrast for the top and bottom carbon layers (**Fig. 2d**). A line profile extracted from the EPI image across a representative atom pair (**Fig. 2e)** reveals two distinct peaks of opposite signs separated by 0.51 Å, whereas the corresponding line profile from the phase image shows strong overlap.

The advantage of EPI becomes even more pronounced in AA-stacked regions, where the two graphene layers overlap almost perfectly in projection. In this case, even the super-resolution ptychography phase imaging fails to resolve the overlapping atoms (**Fig. 2f**), whereas EPI unambiguously resolves all atoms and reveals a vortex-like contrast pattern reflecting the relative twist between the two graphene layers (**Fig. 2g**). This behavior is further demonstrated by the line profiles across a representative atom pair in this region of heavy overlap (marked with arrows in **Fig. 2f, g**): the line profile from EPI image shows two opposite peaks separated by ~0.37 Å that remain distinct, whereas the one from the phase image displays only one broad peak (**Fig. 2h**). Because 2D materials have well-defined axial spacing between overlapping sites due to crystallographic constraints, such interference-derived EPI contrast reliably encodes axial information with improved lateral resolution, as further illustrated by simulations (**Supplementary Fig. 6**).

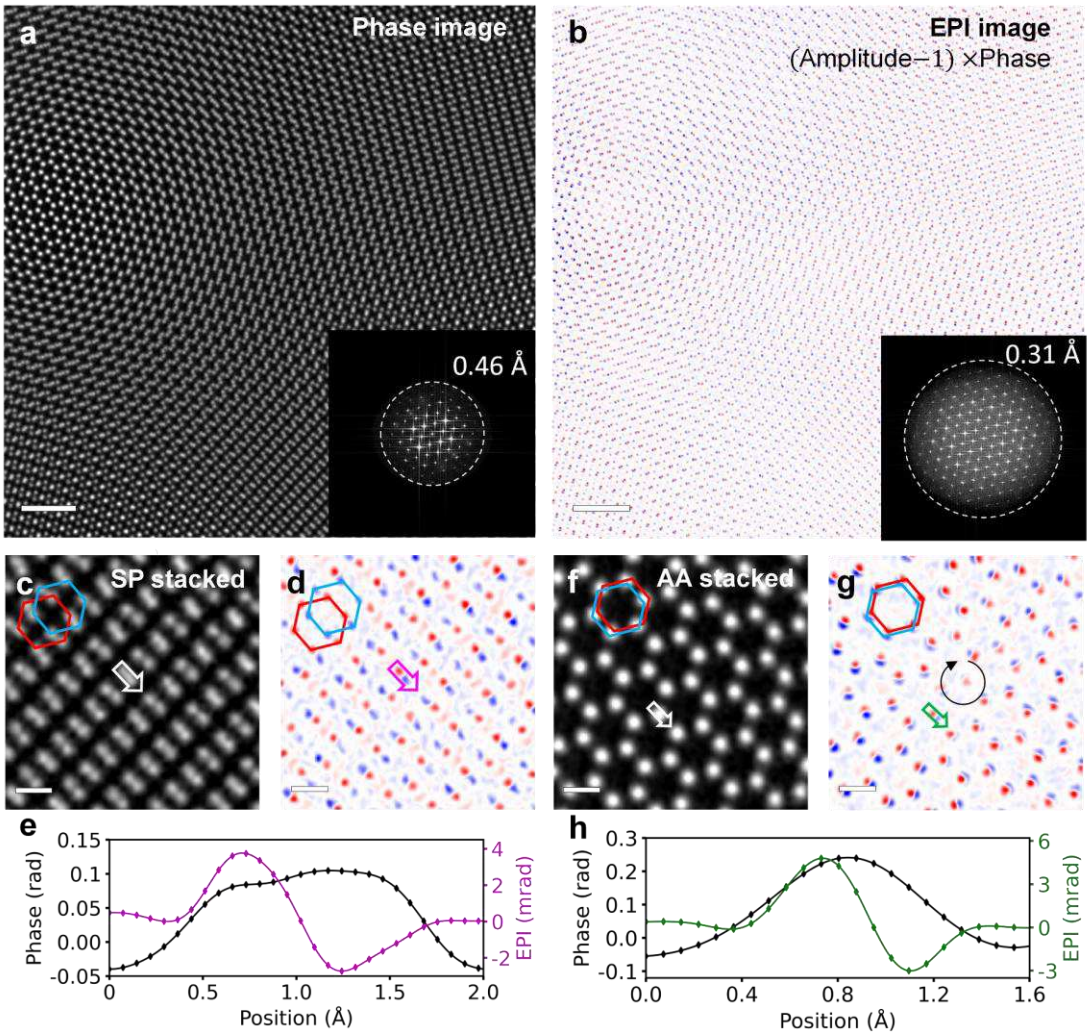


Figure 2. EPI reveals depth-resolved atomic structure in twisted bilayer graphene (tBLG). a-b, Ptychographic phase (a) and corresponding EPI (b) images of a tBLG sample with ~1° twist angle. Insets show the corresponding FFTs. **c-e**, Phase (c) and EPI (d) images of a SP-stacked region. White and pink arrows mark the atom pair whose line profiles are shown in **e**. The EPI profile (pink) exhibits two peaks of opposite sign separated by ~0.51 Å, demonstrating enhanced lateral resolving power and direct encoding of depth information. **f-h**, Phase (f) and EPI (g) images of an AA-stacked region. White and green arrows indicate the atom pair whose line profiles are shown in **h**. The EPI profile reveals two distinct peaks of opposite sign separated by ~0.37 Å, which remain clearly resolved despite strong projection overlap. The clockwise black arrow in **g** marks the vortex-like contrast pattern in the EPI image, reflecting the local twist between the two graphene layers. Scale bars: 1 nm (b, c), 0.2 nm (d, e, g, h).

Quantitative 3D validation on monolayer MoS_2

To quantitatively validate the axial precision of EPI, we applied the method to a monolayer MoS_2 sample intentionally tilted with respect to the incident beam. **Figure 3a** shows the ptychographic phase image, where the separation of S atom pairs in projection reflects the geometric tilt in addition to local lattice corrugation. The corresponding EPI image (**Fig. 3b**) exhibits opposite contrast polarities for S atoms in the upper and lower sub-layers, confirming that EPI directly captures the relative axial position of individual atomic sites. This contrast inversion is also reproduced in simulated 4D-STEM datasets generated under similar conditions (**Supplementary Fig. 7**). Single S vacancies, marked by arrows and dashed circles in the insets of **Fig. 3a, b,** further illustrate the depth sensitivity of EPI: vacancies located in either sub-layer are unambiguously identified by the absence of the corresponding opposite EPI contrast. Quantification reveals that the two S sub-layers contain comparable concentration of S vacancies (3% in the upper and 4% in the lower layer, **Fig. 3c**).

To extract the quantitative 3D coordinates, local contrast maxima in the phase and EPI images were fitted using Gaussian functions. By combining the fitted peak parameters with the calibration between the normalized amplitude change and the z-axis atomic position, we obtain the full 3D coordinates of all S atoms (see **Supplementary Note 2** and **Supplementary Fig. 8** for details). Within each S atom pair, the interlayer S-S distance calculated from the reconstructed 3D coordinates shows an average value of 2.98 Å (**Supplementary Fig. 8b**), in excellent agreement with the known crystallographic spacing of 2.98 Å.

Although the Gaussian peak fitting method is easy to implement and provides a straightforward validation of accuracy, it does not fully exploit the intrinsic correlation between amplitude and phase signals and becomes less reliable in regions where projected phase peaks from different atomic layers overlap. To achieve higher precision and robustness, we developed a wave-propagation-based fitting algorithm that

simultaneously fits both the phase and EPI images (**Fig. 3d**). Using the reconstructed probe functions from the experimental dataset, we model the interference modulated object functions generated by Gaussian-shaped phase atoms and refine the 3D atomic coordinates by minimizing a combined loss function defined over both phase and EPI contrasts (see **Supplementary Note 3** for details). **Figure 3e** shows the histogram of interlayer S-S distances extracted from the refined 3D coordinates, with a mean value of 2.98±0.10 Å. Note that the 10 pm standard deviation reflects the combined fitting uncertainty in all three spatial dimensions as well as intrinsic fluctuations of atomic positions. These results thus demonstrate that EPI achieves picometer-level accuracy in reconstructing 3D atomic coordinates from a single 4D-STEM acquisition.

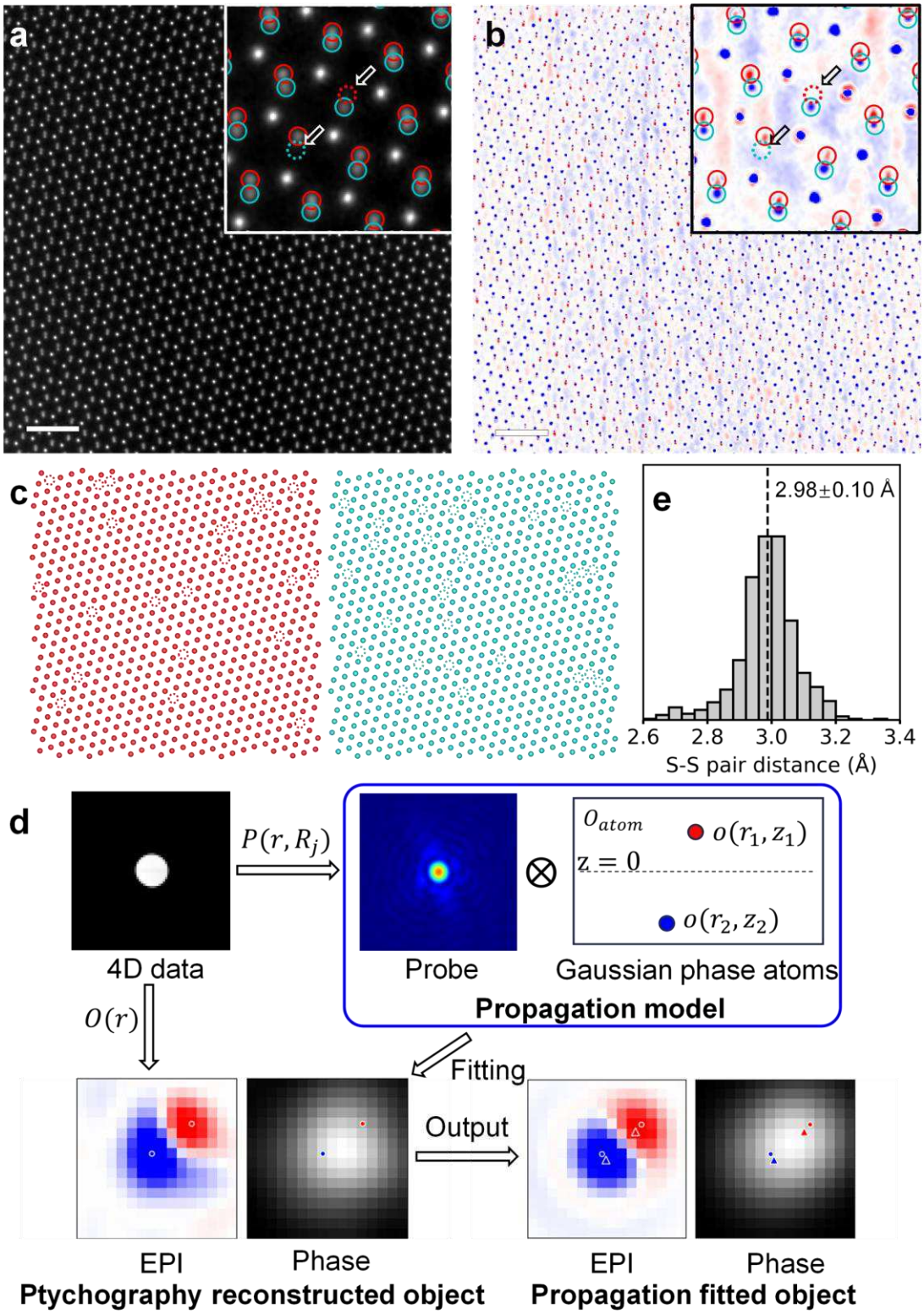


Figure 3. Quantitative 3D validation of EPI on monolayer MoS_2. a-b, Ptychographic phase (a) and EPI (b) images of a tilted monolayer MoS_2 sample. Insets show magnified views in which the upper and lower S sub-layers are marked with red

and blue circles, respectively. Two single S vacancies are marked with arrows and dashed circles. **c,** Structure models of the upper (left, red) and lower (right, blue) S sub-layers, with the identified S vacancies highlighted by dashed circles. The measured S vacancy concentrations are similar in the two S sub-layers. **d,** Schematic of the wave-propagation-based 3D coordinates fitting algorithm. The ptychographically reconstructed probe function interacts with Gaussian-shaped phase atoms and propagates to the reference plane, resulting in a simulated object function. The atomic coordinates are obtained by minimizing a joint loss function defined over both the phase and EPI contrast differences between the simulated and experimentally reconstructed object. Circles in the phase and EPI images denote initial guesses, obtained using the local minima and maxima of the EPI image, and triangles represent fitted atom positions with sub-pixel precision. **e,** Histogram of the interlayer S-S pair distances extracted from the refined 3D coordinates, showing a mean distance of 2.98±0.10 Å, in excellent agreement with the crystallographic value 2.98 Å. Scale bars: 1 nm (a, b).

Quantitative analysis of 3D structural relaxations in tBLG

Having established the quantitative accuracy of EPI, we applied it to tBLG to resolve its intrinsic 3D structural relaxation. **Figure 4a** shows the reconstructed phase image of a tBLG sample with ~1° twist angle (measured from the moiré lattice parameters, **Supplementary Fig. 9a**), displaying distinct AA, AB, and SP stacked regions (see **Supplementary Fig. 10** for the EPI image). The 3D atomic coordinates were extracted from EPI fitting and refined by local averaging with the three nearest in-plane neighbors to reduce stochastic uncertainty (**Supplementary Note 3**). The resulting interlayer-spacing map (**Fig. 4b**), calculated from the reconstructed 3D coordinates, reveals systematic variations across the moiré superlattice, with local expansions near the AA-stacked regions. Mapping of the local twist angles (**Fig. 4c**) also reveals significantly increased in-plane twist in the AA-stacked regions relative to the global interlayer twist, consistent with prior theoretical[14] and experimental[16] reports of coupled in-plane and out-of-plane relaxation in small-angle tBLG.

Quantitatively, the interlayer spacing in the AA-stacked region is larger by approximately 5~7 pm compared with the AB and SP regions (**Fig. 4d**), in agreement with previous theoretical predictions[10,11,13]. The standard deviation of 2~3 pm within each stacking region reflects the intrinsic depth precision of the EPI method. The z-coordinate maps of individual graphene layers further indicates that most of the out-of-plane structural reconstruction in the AA-stacked region originates from axial displacement of one graphene layer, while the other exhibits only random fluctuations (**Fig. 4e**). Similar structural relaxation behavior was consistently observed in additional datasets collected from nearby regions of the same sample (**Supplementary Fig. 11**), demonstrating reproducibility. Previous theoretical studies have predicted that, in small-angle tBLG, two distinct out-of-plane reconstruction modes can occur with comparable energies: a breathing mode, in which both layers in the AA regions bulge outward into vacuum, and a bending mode, where both layers in the AA regions bulge in the same direction[12,13]. The relaxation behaviors observed in our experiment most likely arise from the competition between these two energetically similar modes.

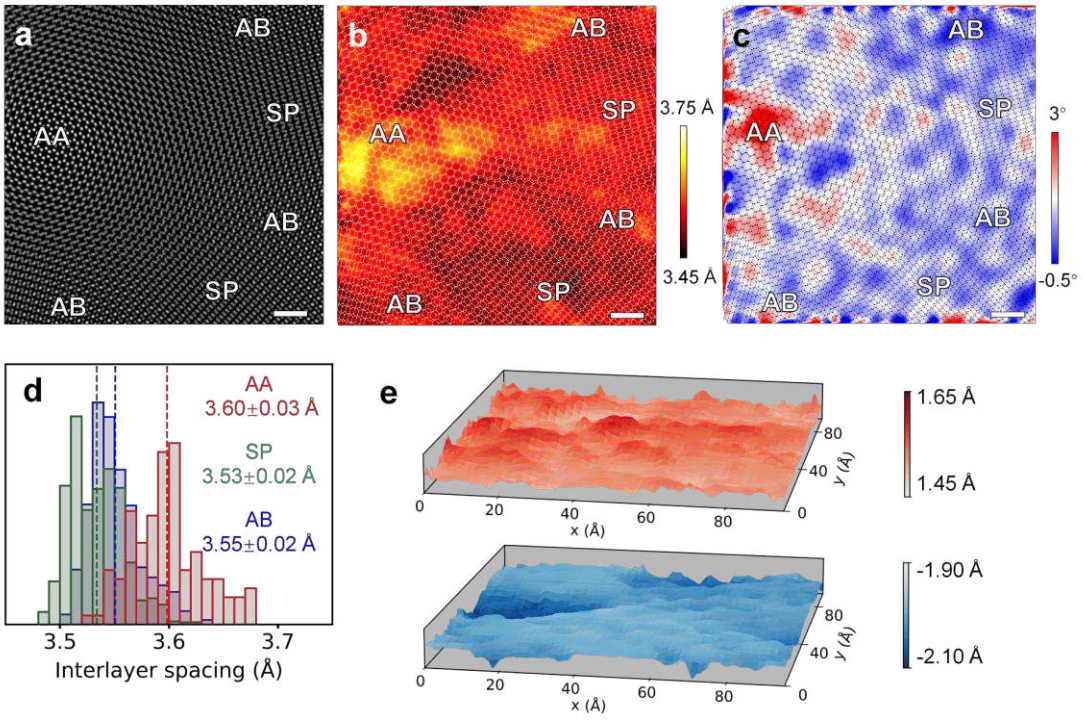


Figure 4. 3D structural relaxation of tBLG revealed by EPI. a-c, Reconstructed phase image (a), interlayer spacing map (b) and local twist angle map (c) of a tBLG sample with ~1° twist angle. EPI-derived 3D coordinates reveal enlarged interlayer spacing and increased in-plane local twist angle at the AA-stacked regions, indicative of coupled out-of-plane and in-plane relaxation. **d,** Histogram of interlayer spacings in AA, AB and SP regions. The AA-stacked region shows a 5~7 pm larger interlayer spacing than AB/SP regions, consistent with theoretical prediction of enhanced out-of-plane structural relaxation at small twist angles. **e,** The z-coordinate maps of the upper (top) and lower (bottom) graphene layers. The relaxation originates mainly from displacement of one layer, while the other exhibits only non-stacking-specific fluctuations. Scale bars: 1 nm (a-c).

We further examined the out-of-plane structural relaxation in a tBLG sample with a larger twist angle of 2.8° (**Supplementary Fig. 9b and Supplementary Fig. 12**). Within the field of view, three AA-stacked regions are clearly visible, all exhibiting a slightly larger interlayer spacing than the surrounding AB and SP regions (**Supplementary Figs. 12b, d**). The corresponding histogram of interlayer spacing (**Supplementary Fig. 12c**) shows that the AA-stacked regions have an average separation of 3.39±0.01 Å, less than 1 pm larger than that of the AB/SP regions. This markedly weaker out-of-plane relaxation compared to the ~1° tBLG sample is expected, as the out-of-plane reconstruction diminishes with increasing twist angle[10,11].

Discussion and outlook

EPI is not limited to pristine crystalline lattices or specific material systems, but is broadly applicable to a wide range of structural problems. **Supplementary Fig. 13** shows that EPI unambiguously resolves the 3D bonding configuration of individual silicon dopants in monolayer graphene, revealing that the threefold-coordinated Si dopant (Si-C_3) exhibits a pronounced out-of-plane buckling, whereas the fourfold-coordinated Si dopant (Si-C_4) remains nearly coplanar with the graphene lattice, in

agreement with theoretical predictions[5,9]. **Supplementary Fig. 14** further demonstrates that EPI can clearly visualize a monolayer amorphous carbon (MAC) structure, composed of 5-6-7-8-membered rings[41-43], on top of a much heavier monolayer MoS_2 via its distinct interferometric signature, highlighting the intrinsic surface sensitivity of this technique.

Recent developments in electron ptychography and tomography have begun to probe 3D atomic structures, yet they still face intrinsic trade-offs among spatial resolution, acquisition time, and experimental complexity. In a recent study, Kim *et al.* [44] applied ptychographic tomography to tBLG with a ~2° twist angle and reported an interlayer expansion of ~4 pm in the AA-stacked regions. However, this tomography approach required extensive tilt-series acquisition and is therefore susceptible to dynamical structural fluctuations and cumulative alignment errors across tilts. Similarly, tilt-coupled multi-slice ptychography can achieve high axial resolution using only a limited number of tilts[39], but accurate spatial registration among datasets remains challenging and limits its general applicability.

Electron ptychographic interferometry (EPI) overcomes these limitations by recovering full 3D atomic coordinates from a single 4D-STEM acquisition, without sample tilting or reliance on prior structural models. Critically, EPI does not infer the third dimension through geometrical parallax, but instead exploits intrinsic wave interference induced by individual atoms, making it fundamentally distinct from all tomography-based approaches. As a result, EPI avoids dose accumulation, reconstruction artifacts, and dynamic structural relaxation that often limit tomography-based techniques, while simultaneously maintaining deep sub-angstrom lateral resolution and picometer axial precision.

The interferometric principle underlying EPI is general and not restricted to atomically thin specimens. The key physical mechanism, i.e. the depth-dependent amplitude-phase

coupling in the electron exit wave, is intrinsic to electron scattering and persists regardless of specimen thickness. In thicker specimens, this information becomes more complex but remains, in principle, recoverable. Multi-slice electron ptychography (MEP) provide a computational framework for recovering this depth-resolved information, even though existing MEP algorithms commonly rely on regularization to stabilize reconstruction[25,32,45], which artificially reduces the independence among adjacent slices. Developing reconstruction strategies that explicitly preserve slice independence while incorporating the quantitative amplitude-phase relationships revealed by EPI represents a promising direction for future work.

In summary, EPI transforms atom-induced wavefront curvature and interference into a quantitative 3D atomic imaging contrast. By harnessing the amplitude information that has traditionally been discarded, EPI overcomes the long-standing axial resolution barrier of conventional electron microscopy. The ability to achieve picometer-precision 3D atomic imaging from a single 4D-STEM acquisition makes EPI particularly powerful for investigating beam-sensitive and dynamically evolving quantum materials. More broadly, the concept of interferometric depth encoding within the electron wavefunction establishes a new paradigm for depth-sensitive microscopy. Integrating this physical insight with multi-slice or tomographic reconstruction frameworks could ultimately extend atomic-resolution 3D imaging to a wider class of materials, enabling a more complete atomic-scale understanding of structure-property relationships in condensed matter systems.

Reference

1 Cao, Y. *et al.* Unconventional superconductivity in magic-angle graphene superlattices. *Nature* **556**, 43-50 (2018).

2 Nuckolls, K. P. & Yazdani, A. A microscopic perspective on moiré materials. *Nat. Rev. Mater.* **9**, 460-480 (2024).

3 Yadav, A. K. *et al.* Observation of polar vortices in oxide superlattices. *Nature* **530**, 198-201 (2016).

4 Banhart, F., Kotakoski, J. & Krasheninnikov, A. V. Structural defects in graphene. *Acs Nano* **5**, 26-41 (2011).

5 Zhou, W. *et al.* Direct determination of the chemical bonding of individual impurities in graphene. *Phys. Rev. Lett.* **109**, 206803 (2012).
6 Lin, J. H. *et al.* AC/AB stacking boundaries in bilayer graphene. *Nano Lett.* **13**, 3262-3268 (2013).
7 Novoselov, K. S., Mishchenko, A., Carvalho, A. & Neto, A. H. C. 2D materials and van der Waals heterostructures. *Science* **353**, 7 (2016).
8 Ge, Y. Y. *et al.* Two-dimensional nanomaterials with unconventional phases. *Chem* **6**, 1237-1253 (2020).
9 Xu, M. Q. *et al.* Single-atom vibrational spectroscopy with chemical-bonding sensitivity. *Nat. Mater.* **22**, 612-618 (2023).
10 Uchida, K., Furuya, S., Iwata, J. I. & Oshiyama, A. Atomic corrugation and electron localization due to moiré patterns in twisted bilayer graphenes. *Phys. Rev. B* **90**, 155451 (2014).
11 van Wijk, M. M., Schuring, A., Katsnelson, M. I. & Fasolino, A. Relaxation of moire patterns for slightly misaligned identical lattices: graphene on graphite. *2D Mater.* **2**, 034010 (2015).
12 Dai, S. Y., Xiang, Y. & Srolovitz, D. J. Twisted bilayer graphene: Moiré with a twist. *Nano Lett.* **16**, 5923-5927 (2016).
13 Rakib, T., Pochet, P., Ertekin, E. & Johnson, H. T. Corrugation-driven symmetry breaking in magic-angle twisted bilayer graphene. *Commun. Phys.* **5**, 242 (2022).
14 Yoo, H. *et al.* Atomic and electronic reconstruction at the van der Waals interface in twisted bilayer graphene. *Nat. Mater.* **18**, 448-453 (2019).
15 Park, D. *et al.* Unconventional domain tessellations in moiré-of-moiré lattices. *Nature* **641**, 896–903 (2025).
16 Kazmierczak, N. P. *et al.* Strain fields in twisted bilayer graphene. *Nat. Mater.* **20**, 956-963 (2021).
17 Zhang, Y. C. *et al.* Atom-by-atom imaging of moiré phasons with electron ptychography. *Science* **389**, 423-428 (2025).
18 Rodenburg, J. M. & Bates, R. H. T. The theory of super-resolution electron microscopy via Wigner-distribution deconvolution. *Philos. Trans. R. Soc. A-Math. Phys. Eng. Sci.* **339**, 521-553 (1992).
19 Miao, J. W. Computational microscopy with coherent diffractive imaging and ptychography. *Nature* **637**, 281-295 (2025).
20 Stephen J. Pennycook, R. I., Haijun Wu, Xiaoxu Zhao, Changjian Li, Duane Loh, Jiadong Dan, & Zhou, W. Physics through the microscope. *Chin. Phys. B* **33**, 116801 (2024).
21 Batson, P. E., Dellby, N. & Krivanek, O. L. Sub-angstrom resolution using aberration corrected electron optics. *Nature* **418**, 617-620 (2002).
22 Krivanek, O. L. *et al.* Atom-by-atom structural and chemical analysis by annular dark-field electron microscopy. *Nature* **464**, 571-574 (2010).
23 Li, A. W., Li, A. & Zhou, W. Low-voltage single-atom electron microscopy with carbon-based nanomaterials. *Micron* **186**, 103706 (2024).

24 Jiang, Y. *et al.* Electron ptychography of 2D materials to deep sub-angstrom resolution. *Nature* **559**, 343-349 (2018).
25 Chen, Z. *et al.* Electron ptychography achieves atomic-resolution limits set by lattice vibrations. *Science* **372**, 826-831 (2021).
26 Yang, W. F., Sha, H. Z., Cui, J. Z., Mao, L. Z. & Yu, R. Local-orbital ptychography for ultrahigh-resolution imaging. *Nat. Nanotechnol.* **19**, 612–617 (2024).
27 Sha, H. Z., Cui, J. Z. & Yu, R. Deep sub-angstrom resolution imaging by electron ptychography with misorientation correction. *Sci. Adv.* **8**, eabn2275 (2022).
28 Nguyen, K. X. *et al.* Achieving sub-0.5-angstrom-resolution ptychography in an uncorrected electron microscope. *Science* **383**, 865-870 (2024).
29 Borisevich, A. Y., Lupini, A. R. & Pennycook, S. J. Depth sectioning with the aberration-corrected scanning transmission electron microscope. *Proc. Natl. Acad. Sci. U. S. A.* **103**, 3044-3048 (2006).
30 Xin, H. L., Intaraprasonk, V. & Muller, D. A. Depth sectioning of individual dopant atoms with aberration-corrected scanning transmission electron microscopy. *Appl. Phys. Lett.* **92**, 013125 (2008).
31 Ishikawa, R., Shibata, N., Taniguchi, T. & Ikuhara, Y. Three-dimensional imaging of a single dopant in a crystal. *Phys. Rev. Appl.* **13**, 034064 (2020).
32 O'Leary, C. M. *et al.* Three-dimensional structure of buried heterointerfaces revealed by multislice ptychography. *Phys. Rev. Appl.* **22**, 014016 (2024).
33 Scott, M. C. *et al.* Electron tomography at 2.4-angstrom resolution. *Nature* **483**, 444–447 (2012).
34 Miao, J., Ercius, P. & Billinge, S. J. L. Atomic electron tomography: 3D structures without crystals. *Science* **353**, aaf2157 (2016).
35 Busch, R., Rez, P., Treacy, M. M. J. & Zuo, J.-M. Limit of atomic-resolution-tomography reconstruction of amorphous nanoparticles. *Nature* **649**, 1119-1122 (2026).
36 Liao, Y. *et al.* Accurate determination of the 3D atomic structure of amorphous materials. *Nature* **649**, 1123-1129 (2026).
37 Pelz, P. M. *et al.* Solving complex nanostructures with ptychographic atomic electron tomography. *Nature Communications* **14**, 7906 (2023).
38 Hofer, C., Mustonen, K., Skákalová, V. & Pennycook, T. J. Picometer-precision few-tilt ptychotomography of 2D materials. *2D Mater.* **10**, 035029 (2023).
39 Dong, Z. H. *et al.* Sub-nanometer depth resolution and single dopant visualization achieved by tilt-coupled multislice electron ptychography. *Nature Communications* **16**, 1219 (2025).
40 Tian, X. Z. *et al.* Correlating the three-dimensional atomic defects and electronic properties of two-dimensional transition metal dichalcogenides. *Nat. Mater.* **19**, 867-873 (2020).
41 Toh, C. T. *et al.* Synthesis and properties of free-standing monolayer amorphous carbon. *Nature* **577**, 199-203 (2020).
42 Tian, H. F. *et al.* Disorder-tuned conductivity in amorphous monolayer carbon. *Nature* **615**, 56-61 (2023).

43 Bai, X. H. *et al.* Nitrogen-doped amorphous monolayer carbon. *Nature* **634**, 80-84 (2024).

44 Kim, N. Y. *et al.* Determining 3D atomic coordinates of light-element quantum materials using ptychographic electron tomography. arXiv:2504.08228 (2025).

45 Lee, C. H., Zeltmann, S. E., Yoon, D., Ma, D. S. & Muller, D. A. PtyRAD: A high-performance and flexible ptychographic reconstruction framework with automatic differentiation. *Microsc. microanal.* **31**, ozaf070 (2025).

Methods

Sample growth and preparation

Twisted bilayer graphene (tBLG) samples were fabricated using the conventional tear-and-stack method[46]. A sharp tip was used to tear the mechanically exfoliated monolayer graphene into two parts. One half was picked up with a polyvinyl alcohol (PVA) membrane supported on a polydimethylsiloxane (PDMS) stamp and then stacked on the other half with a controlled twist angle. MoS_2 samples were grown via CVD in a single-temperature-zone tube furnace with SiO_2/Si substrate using MoO_3 and S powder. The as-grown MoS_2 layer was transferred to a TEM grid using a polymethyl-methacrylate (PMMA)-assisted method.

4D-STEM experiments

The 4D-STEM experiments were performed on an aberration-corrected Nion U-HERMES 100 microscope operated at 60 kV, using a convergence semi-angle of 32 mrad and a beam current of about 10 pA. 4D-STEM datasets were acquired using a DECTRIS ELA hybrid pixel detector with a 128×128 readout area and maximum collection semi-angle of ~170 mrad. A defocus condition of approximately 5 nm was used. For the ~1° tBLG sample and monolayer MoS_2 sample, the scanning steps was 0.05 nm with a scanning array of 200×200. For the 2.8° tBLG sample, the scanning steps was 0.04 nm with a scanning array of 256×256.

Electron Ptychographic Interferometry

Ptychographic reconstructions were performed with PtychoShelves[47] based fold-slice package[25]. The reconstructions used the least-squares maximum-likelihood algorithm[48], mixed-states ptychography[49] and scan position correction. Before reconstruction, the convergent beam electron diffraction (CBED) patterns were zero-padded to 256×256 pixels, corresponding to ~7 pm real-space pixel size. After reconstruction, the amplitude image was normalized by subtracting unity to remove the unscattered reference wave and then multiplied by the corresponding phase image to obtain the EPI

image. The resulting amplitude–phase product constitutes the interferometric contrast $EPI\ (r) = [A(r) - 1] \times \phi(r)$, which retains amplitude-derived depth information and enhances lateral sharpness.

4D-STEM simulations

The 4D-STEM simulations were conducted using abTEM python package[50]. 60 kV acceleration voltage, 32 mrad convergence semi-angle, 100 mrad collection angle, and 0.5 Å scan step size was used to match the experimental conditions. Poisson noised was added before ptychography reconstruction, assuming a dose of $2 \times 10^8\ e^-/\text{Å}^2$ for monolayer MoS_2 and $2 \times 10^9\ e^-/\text{Å}^2$ for tBLG. Ptychographic reconstructions were then performed using the same processing procedure as the experimental data, except that mixed probe states and scan position corrections were omitted.

Determination of different stacking regions in tBLG

The carbon hexagons in each graphene layer were first identified based on atomic coordination, and the displacement vector of each hexagon relative to its nearest neighbor in the other layer was calculated. Stacking (AA, SP and AB) types were then determined by the displacement vectors (**Supplementary Fig. 13c**): regions with displacement magnitude less than 0.4 Å were classified as AA-stacked, and those with displacement magnitude larger than 0.9 Å were assigned as AB or SP stacked. SP/AB stacking were separated by the direction of displacement vectors: regions with displacement vectors oriented within 10° of the carbon lattice directions are assigned as AB, and those with displacement vectors oriented within 10° of the hexagon lattice directions (60° offset from the carbon lattice) are assigned as SP. The transitional regions between AB and SP, as well as the transitional regions between AA and SP/AB stacked regions with displacement magnitude of 0.4~0.9 Å, were excluded from the statistics to avoid additional distribution broadening.

References for Methods:

46 Kim, K. *et al.* van der Waals Heterostructures with High Accuracy Rotational Alignment. *Nano Lett.* **16**, 1989-1995 (2016).

47 Wakonig, K. *et al.* PtychoShelves, a versatile high-level framework for high-performance analysis of ptychographic data. *J. Appl. Crystallogr.* **53**, 574-586 (2020).

48 Odstrcil, M., Menzel, A. & Guizar-Sicairos, M. Iterative least-squares solver for generalized maximum-likelihood ptychography. *Opt. Express* **26**, 3108-3123 (2018).

49 Thibault, P. & Menzel, A. Reconstructing state mixtures from diffraction measurements. *Nature* **494**, 68-71 (2013).

50 Madsen, J. & Susi, T. The abTEM code: transmission electron microscopy from first principles. *Open research Europe* **1**, 24 (2021).

Acknowledgements

We thank Dr. Timothy Pennycook for providing valuable comments on the manuscript. This research was supported by the Chinese Academy of Sciences, the Beijing Outstanding Young Scientist Program (BJJWZYJH01201914430039), and the National Natural Science Foundation of China (grant no. 62488201). This research benefited from resources and supports from the Electron Microscopy Center at the University of Chinese Academy of Sciences.

Author contributions

W.Z. designed and supervised the research. A.L. performed the STEM experiments and ptychographic reconstruction, proposed the EPI mechanism and completed the simulation verification. S.H. wrote the code of propagation fitting model and performed the coordinates analysis. Y.M. obtained the first identification of depth information in the amplitude image. Z.W. prepared the tBLG samples and J.P. prepared the MoS_2 sample. T.L. contributed to the data processing. S.J.P. and H.-J.G. provided valuable discussion and suggestions. A.L., S.H. and W.Z. wrote the paper. All authors discussed the results and commented on the paper.

Competing interests

The authors declare no competing interests.

Data availability

The data that support the findings of this study are available from the corresponding authors on reasonable request.

Code availability

The code for electron ptychography reconstruction is adapted from the open-source fold_slice package. Other codes that support the findings of this study, including codes

for wave propagation simulation, EPI contrast analysis and 3D coordinates fitting models, will be publicly available upon publication.

Supplementary Files

This is a list of supplementary files associated with this preprint. Click to download.

- EPISupplementaryInformation.docx